Nanoscale

PAPER

View Article Online
View Journal | View Issue

Cite this: *Nanoscale*, 2018, **10**, 21871

A needle-like optofluidic probe enables targeted intracellular delivery by confining light-nanoparticle interaction on single cell†

Andrew Doppenberg,[a,b] Michel Meunier [c] and Christos Boutopoulos *[a,d,e]

Received 14th May 2018,
Accepted 10th November 2018

DOI: 10.1039/c8nr03895c

rsc.li/nanoscale

Intracellular delivery of molecular cargo is the basis for a plethora of therapeutic applications, including gene therapy and cancer treatment. A very efficient method to perform intracellular delivery is the photo-activation of nanomaterials that have been previously directed to the cell vicinity and bear releasable molecular cargo. However, potential *in vivo* applications of this method are limited by our ability to deliver nanomaterials and light in tissue. Here, we demonstrate intracelullar delivery using a needle-like optofluidic probe capable of penetrating soft tissue. Firstly, we used the optofluidic probe to confine an intracellular delivery mixture, composed of 100 nm gold nanoparticles (AuNP) and membrane-impermeable calcein, in the vicinity of cancer cells. Secondly, we delivered nanosecond (ns) laser pulses (wavelength: 532 nm; duration: 5 ns) using the same probe and without introducing a AuNP cells incubation step. The AuNP photo-activation caused localized and reversible disruption of the cell membrane, enabling calcein delivery into the cytoplasm. We measured 67% intracellular delivery efficacy and showed that the optofluidic probe can be used to treat cells with single-cell precision. Finally, we demonstrated targeted delivery in tissue (mouse retinal explant) *ex vivo*. We expect that this method can enable nanomaterial-assisted intracellular delivery applications in soft tissue (*e.g.* brain, retina) of small animals.

Introduction

The membrane of a live cell is a selectively permeable barrier that separates physically the intracellular components from the surrounding extracellular environment. A plethora of cellular engineering and therapeutic approaches are based on the ability to introduce extracellular substances, otherwise membrane-impermeable, into the cytoplasm, including proteins[1,2] and plasmids.[3,4] Notable therapeutic applications include gene therapy of vision diseases[4] and cancer treatment.[5]

In both clinical and preclinical studies, viral vectors are the most commonly used vehicles for intracellular delivery of plasmids for gene silencing and editing.[6] Nevertheless, viral vector-based approaches are limited by high costs and major safety concerns.[7] A growing research effort is directed towards the development of alternative, non-viral intracellular delivery platforms, including the use of nanomaterials.[8] Nanomaterials have been shown to be unique vehicles for intracellular delivery because of their ability to (i) penetrate the cell membrane *via* endocytosis pathways,[9] (ii) bear cell targeting ligands,[10] and (iii) releasable molecular cargo.[11] Moreover, nanomaterials have tunable optical properties, enabling controlled intracellular release of molecular cargo *via* photo-activation pathways.[12]

The use of a pulsed laser to photo-activate nanomaterials–cell complexes minimizes excess collateral heating and prevents compromisation of cell viability. More specifically, the interaction of nanomaterials with pulsed lasers can generate a variety of stimulus at the nanoscale, including localized heating, plasma generation, cavitation and transient nanobubble generation.[13,14] Importantly, laser parameters and nanomaterial properties can be appropriately rationalized to favour the desired stimulus.[15–17] The confinement of such stimulus to the membrane of a live cell can lead to localized and reversible membrane disruption, enabling intracellular delivery. Several groups have successfully employed this method to perform intracellular delivery of molecular cargo such as dyes,[18–23] siRNA[23,24] and plasmids.[20,23]

Even though numerous *in vitro* studies have shown efficient intracellular delivery with photoactivatable nanomaterials, certain limitations set barriers for *in vivo* applications. First, *in vivo* cell targeting efficiency has been

[a]*Maisonneuve-Rosemont Hospital Research Centre, Montreal, Quebec, Canada. E-mail: christos.boutopoulos@umontreal.ca*
[b]*Faculty of Applied Science, University of British Columbia, Vancouver, British Columbia, Canada*
[c]*Laser Processing and Plasmonics Laboratory, Polytechnique Montréal, Montreal, Quebec, Canada*
[d]*Department of Ophthalmology, University of Montreal, Montreal, Quebec, Canada*
[e]*Institute of Biomedical Engineering, University of Montreal, Montreal, Quebec, Canada*

† Electronic supplementary information (ESI) available: Quantification of apoptotic and necrotic cells (Fig. S1). See DOI: 10.1039/c8nr03895c

proved poor.[25] Indicatively, in a 10-year literature survey, only 0.7% of the administered nanoparticle dose was found to be delivered to a solid tumour.[25] Second, external photo-activation of nanomaterials *in vivo* is limited by the sub-mm penetration depth of light in tissue.[26] There is currently a lack of systems that can potentially address these challenges in tissue.

In this work, we sought the development of such a system based on a needle-like optofluidic probe, capable of penetrating soft tissue. The probe has a dual-core (*i.e.*, optical and hollow), enabling simultaneous light and liquid delivery (Fig. 1). First, we used the probe to deliver an intracellular delivery mixture, composed of 100 nm gold nanoparticles (AuNPs) and a membrane-impermeable dye, in the vicinity of cultured cancer cells and retinal tissue *ex vivo*. Then, we used the same probe to irradiate samples with nanosecond (ns) laser pulses without any previous AuNP incubation step. We report *in situ* measurement of AuNP localization and intracellular delivery of the dye with single-cell precision. Furthermore, we instigated the effect of laser fluence on both intracellular delivery efficacy and cell viability. Finally, we discuss the underlying intracellular delivery mechanism and implications for potential *in vivo* applications.

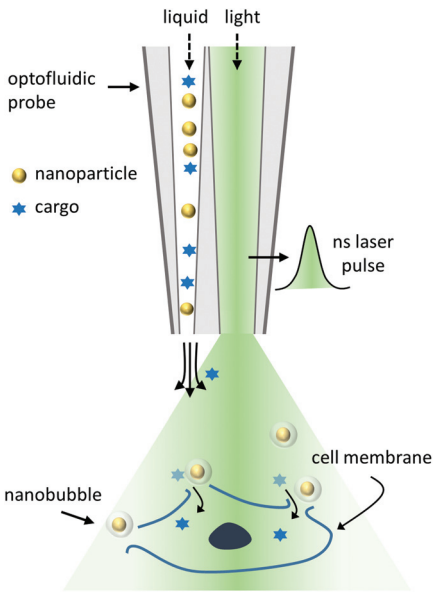

Fig. 1 Schematic overview showing the working principle of the needle-like optofluidic probe. AuNPs and molecular cargo are being delivered at the cell vicinity. Pulsed laser irradiation results in transient nanobubble generation around the AuNPs, enabling delivery of extracellular cargo into the cytoplasm.

Materials and methods

Needle-like optofluidic probes

We used glass optofluidic probes (SQRT, Doric Lenses, Canada) that have a needle-like shape, enabling penetration in soft tissue.[27] The probes are re-usable and consist of a dual-core glass fiber, enabling both light and liquid delivery. The probes were 30–35 mm long and had a non-tapered input end (1 mm in diameter) as well as a tapered tip end for the output (Fig. 2(a)–(c)). Before tapering, the diameter of the optical (graded index, NA = 0.23) and hollow core were 500 μm and 250 μm, respectively. We used optofluidic probes with taper lengths ranging from 3 mm to 5 mm and tapered tip diameters ranging from 30 μm to 100 μm. Note that we also tested thinner optofluidic probes (down to 10 μm) and we observed clogging of the hollow core. Thus, we opted to use probes of at least 30 μm in diameter. The probes were mounted on a holder (SCRH, Doric Lenses, Canada), enabling both light and liquid coupling (Fig. 2(d)). A peristaltic pump was used to pump liquid mixtures *via* the probes. We applied a simple cleaning protocol before and after each use. We first rinsed with ~1 mL of ethanol and then with ~1 mL of deionized water by sucking the liquids through the tapered output tip.

Laser coupling

We used a Nano S 60-30 (Litron, UK) (λ = 532 nm, τ = 5 ns) laser source for our work. The beam delivery system consisted of a 2 m long FC/PC terminated optical fiber cable (FG365UEC, Thorlabs) connected to the optofluidic probe holder. We used

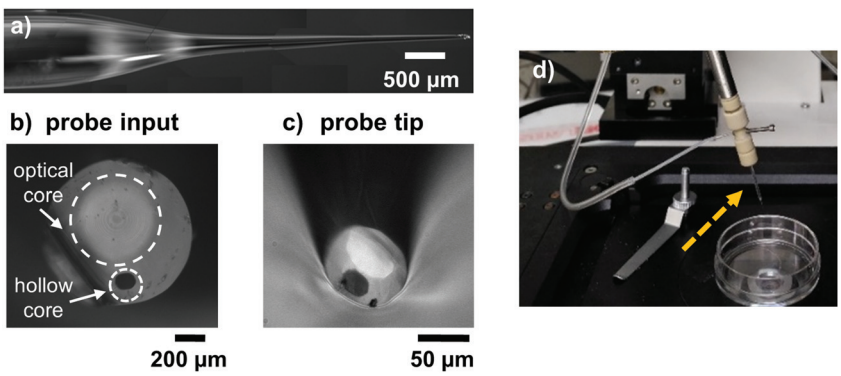

Fig. 2 (a)–(c) Side and cross-section views of a dual-core needle-like optofluidic probe. (d) The setup used for cell treatment. The arrow indicates the probe attached to the probe holder.

a plano convex lens (LA1484-A, Thorlabs) to couple the laser beam to the optical fiber. The overall coupling efficiency (*i.e.*, $E_{\text{probe output}}/E_{\text{fiber input}}$) ranged from 1% to 2% for the various probes tested.

Cell culturing

MDA-MB-231 cells were cultured in Dulbecco's Modified Eagle Medium (DMEM) (Thermo Fisher Scientific) supplemented with antibiotics (100 units per mL penicillin and 100 μg mL^{-1} streptomycin, Thermo Fisher Scientific) and 10% Fetal Bovine Serum (FBS, Thermo Fisher Scientific) in a humidified incubator at 37 °C under a 5% CO_2 atmosphere. For intracellular delivery experiments, we seeded the cells in plastic petri dishes (35 mm). When cells reached ~80% confluence, we washed them once with Leibovitz's L-15 medium without phenol red (Thermo Fisher Scientific) and finally added 2 mL of the same medium for the intracellular delivery experiments.

Cell treatment

The probe holder assembly was mounted on an x–y–z manual translation stage, which was fixed on the main body of an inverted microscope (Observer A1, Zeiss) equipped with a motorized x–y translation stage (MLS203, Thorlabs) (Fig. 2(d)). We used the optofluidic probe to deliver a mixture of 300 μL AuNPs (5.71×10^9 NPs per mL) (A11-100-CIT, Nanopartz) and 25 μL of cell-impermeant green dye (calcein, 16 mM) (C481, Thermo Fisher Scientific) into each petri dish. The flow was set to ~60 μL min^{-1} and the probe was kept at 300 μm above the cell level during the delivery of the mixture. For perforation control experiments, we did not add AuNP into the mixture. After the completion of the mixture delivery, we lowered the probe to 50 μm above the cell level and applied the laser treatment. The laser repetition rate was 20 Hz and the peak laser fluence at the sample level varied from 20 to 200 mJ cm^{-2}. Note that we calculated peak laser fluence as twice the average fluence. The number of pulses per cell was varied from 2 to 100 for single-cell treatment. For treatment of multiple cells, we irradiated several 1 mm × 0.25 mm areas of each petri. We adjusted the translation stage scanning speed and step size so that each cell received an average of 5 pulses. Cells were incubated for 1 h following irradiation (0.5% CO_2–37 °C).

Intracellular delivery, cell necrosis and cell apoptosis quantification

We quantified intracellular delivery of calcein by fluorescence microscopy. We used propidium iodide (PI; red dye; P4170, Sigma) to quantify cell viability post treatment. We added PI to each petri dish 1 h after laser treatment (final concentration: 2.5 μM) to stain cells with compromised membrane integrity.

Finally, we washed the cells twice with L-15 medium before fluorescence imaging. We used ImageJ to calculate the percentage of perforated cells (no. of calcein and PI positive cells/no. of irradiated cells), perforated and live cells (no. of calcein positive and PI negative cells/no. of irradiated cells) and dead cells (no. of PI positive cells/no. of irradiated cells). We defined I_c the fluorescence intensity of an examined cell, $I_{r_{av}}$ the average fluorescence intensity of a reference negative cell and $\sigma_{I_{r_{av}}}$ its standard deviation. We used the following condition to determine positive cells: $I_c \geq I_{r_{av}} + 5 \times \sigma_{I_{r_{av}}}$. For multiple cell treatment experiments, we used a non-treated area of the sample, close to the area of interest, to evaluate the number of irradiated cells. Thus, the reported results account for cell detachment. For single cell treatment experiments, we used images prior to and following treatment to calculate cell detachment. We quantified apoptotic cells with an independent series of experiments without adding calcein after irradiation. We used YOPRO-1 (green dye, Y3603, Thermo Fisher Scientific, final concentration 1 μM) to identify apoptotic and/or necrotic cells and PI to identify necrotic cells, 1 h and 24 h post treatment. For this assay we applied an additional washing step after laser treatment. We quantified ~50 cells per experimental set and performed three independent experiments for each experimental set.

Tissue preparation and treatment

Mouse retinal explants (postnatal day 5) were prepared as previously described.[28] We placed retina quadrants into tissue culture plate well inserts (PIHP03050) with the retinal-ganglion side up and incubated for 1 h before irradiation. We irradiated an 0.5 mm × 0.5 mm area of each retinal explant at 60 mJ cm^{-2}. The perforation mixture injection step and perforation/viability assays were the same as in the 2D cancer cell culture experiments.

Confocal fluorescence microscopy

We used an upright confocal microscope (LSM 880, Axio Examiner, Zeiss) with an immersion objective lens (W Plan-Apochromat 20×/1.0, Zeiss) to perform *in situ* imaging of the AuNPs' localization on the MDA-MB-231 cells. An argon laser (λ = 458) was used to capture green autofluorescence of cells (collection range settings: 489 nm–540 nm) and a HeNe laser (λ = 543 nm) to visualize the AuNPs (collection range settings: 540 nm–550 nm). Note that we used non-fluorescence NPs. These NPs are detectable because they cause enormous elastic scattering of the incident laser beam that is not completely filtered by the dichroic mirror. Note that we also de-activated the laser line filtering module of the microscope to optimize AuNP imaging. *Z*-Stacks of single cells were captured with a 0.5 μm step size. For quantification, we performed three independent experiments.

Results and discussion

Localization of AuNPs

Previous intracellular delivery studies have shown that AuNP generate transient microbubbles upon pulsed laser irradiation.[15,22,29] It has been demonstrated that the proximity of those microbubbles to the cell membrane plays a key role in the perforation mechanism.[22] Therefore, we investigated the localization of AuNPs on the cell membrane after the injection of the intracellular delivery mixture by the optofluidic probe.

Note that our approach does not involve cell incubation with the perforation mixture prior irradiation.

In situ imaging of the AuNP localization on cell membrane was performed by confocal microscopy. We imaged the samples 5 min after injecting the intracellular delivery mixture without the cell-impermeable calcein. Fig. 3 shows indicative imaging planes of a cell. Green indicates cell autofluorescence and red dots indicate AuNPs. We did not observe endocytosis of the AuNP within the examined time frame. The number of AuNPs localized on the cell membrane was 18 ± 2 and no AuNP clustering was observed. To our knowledge, this the first AuNP-assisted intracellular delivery study reporting *in situ* AuNP localization measurements at the exact time frame in which cell irradiation is performed. In previous studies, scanning electron microscopy has been employed to study AuNP localization. This method involves cell fixation and washing steps, and, therefore, presumably underestimates the actual number of AuNPs on cells during the irradiation step. Nevertheless, the measured number of AuNPs per cell in our study (18 AuNPs per cell) is significantly lower compared to previously reported numbers (70 to 250 AuNPs per cell) in relevant studies.[20–22,30] This is attributed to the absence of cells AuNP incubation time in our approach. On the contrary, previous studies employed incubation times ranging from 1 h to 6 h. The ability to attain intracellular delivery with less AuNPs is important considering the reported cell cytotoxicity effects of high AuNP doses.[31,32]

Intracellular delivery in multiple cells

In the first part of our study, we aimed to determine optimum laser fluence for intracellular delivery of calcein. Note that we used multiple optofluidic probes having slightly different tip geometry. The tip geometry strongly affects the exiting beam intensity profile and laser fluence calculation. We accounted for this with the following measurements. Before irradiation, we imaged the exiting beam for each optofluidic probe by acquiring z planes separated by 5 μm. We then reconstructed the 3D profile of the exiting beam and measured (at $1/e^2$) the beam diameter at the sample level (*i.e.*, 50 μm far from the tip,

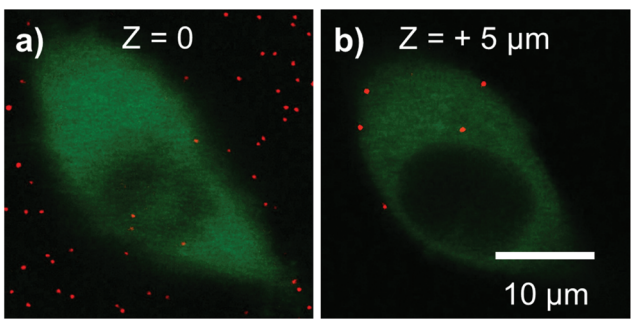

Fig. 3 Confocal fluorescence microscopy images of an MDA-MB-231 cell 5 min after injecting AuNPs. Green indicates cell autofluorescence and red dots AuNP localization. (a) Petri surface level, z = 0, (b) z = 5 μm. The contrast of the red channel has been enhanced to improve the visibility of the AuNPs.

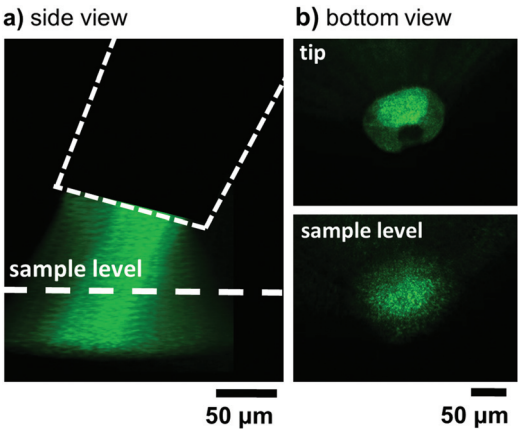

Fig. 4 Optical microscopy images showing the spatial distribution of the laser beam exiting the optofluidic probe. (a) Reconstruction of the sideview profile by using bottom view imaging slices acquired with 5 μm separation distance. (b) Bottom view of the beam at the tip and sample level.

Fig. 4). The diameter varied from 30 μm to 150 μm for the different probes used. For each probe, we adjusted accordingly the scanning speed to perform irradiation overlaps. More specifically, each cell received an average of 5 pulses with at least 80% of the peak fluence. We employed the optofluidic probe to treat multiple stripes in each petri dish (1 mm × 0.25 mm) at different laser fluences. Fig. 5 shows fluorescence microscopy images of treated and non-treated zones, where intracellular delivery is indicated in green and cell death in red. The peak laser fluence was varied from 30 mJ cm^{-2} to 90 mJ cm^{-2}, with the low value representing the intracellular delivery threshold and the high value 100% cell death. Up to 60 mJ cm^{-2}, we observed an increase of the green dye uptake at the irradiated zones with the increase of the laser fluence (Fig. 5). For higher fluences, the dye uptake decreases and significant cell death is observed (Fig. 5). The optimum laser fluence was determined to be 60 mJ cm^{-2}, where perforated cells, living perforated cells, and dead cells represented 77%, 67%, and 23% of the irradiated population, respectively (Fig. 6).

Our control experiment consisted in injecting calcein without AuNPs and irradiating at 400 mJ cm^{-2}, an upper limit imposed by the damage threshold of the coupling optical fibre. We did not observe intracellular delivery, cell death or cell detachment for the control experiment (Fig. 5 and 6). Similarly, we did not observe any noticeable effect on the non-irradiated areas of samples injected with the intracellular delivery mixture (Fig. 5 and 6). Note that green and red cells observed outside of the irradiation zone for high laser fluences (Fig. 5), indicate the effect of the tail of the Gaussian-like beam exiting the optofluidic probe.

We further investigated potential cell stress due to laser treatment by using a dye that stains apoptotic cells (YOPRO-1). We added the dye 1 h and 24 h post treatment to investigate apoptotic behaviour in both short and long-term.

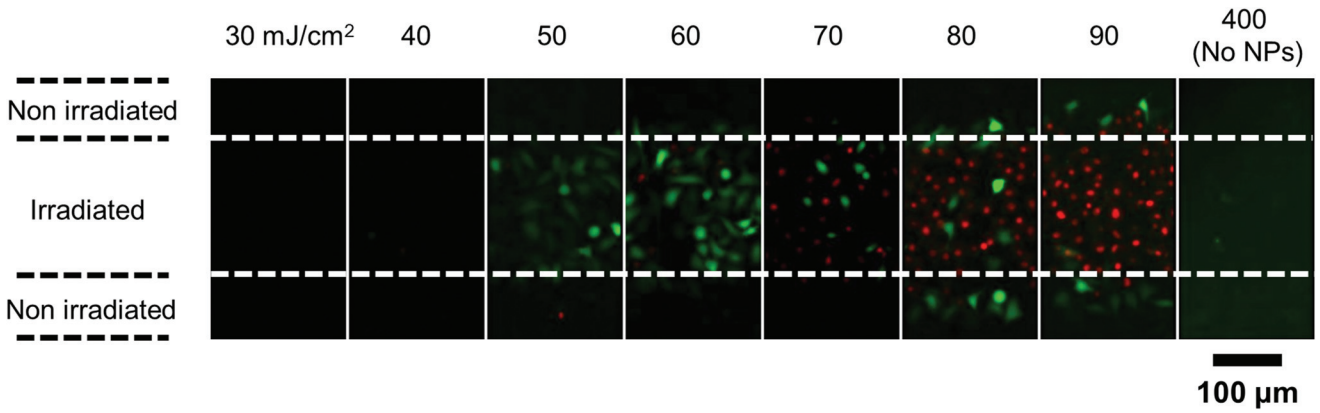

Fig. 5 Fluorescence microscopy images of MDA-MB-231 cells irradiated by an optofluidic probe at laser fluences ranging from 30 to 90 mJ cm^{-2} (intracellular delivery experiments) and 400 mJ cm^{-2} (control experiments). Green staining indicates intracellular delivery and red staining indicates cell death.

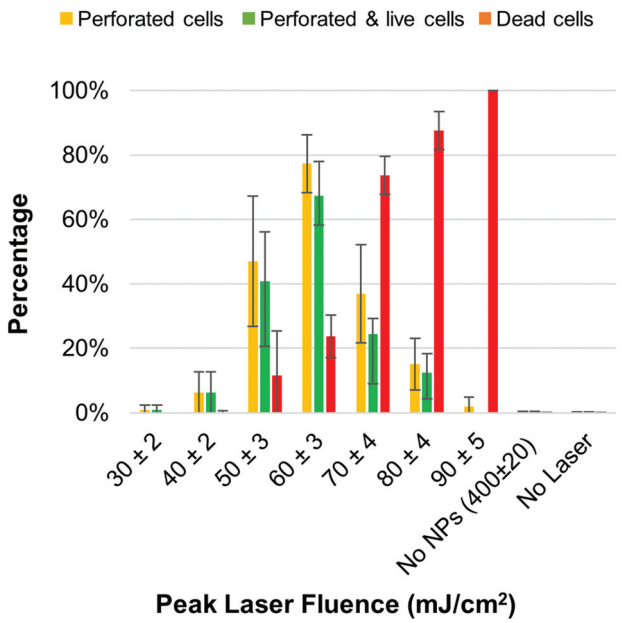

Fig. 6 Intercellular delivery and cell viability percentages as a function of the laser fluence for laser treated, control (no AuNPs) and non-treated samples. The error bars indicate the standard deviation of three independent experiments.

Independently of the laser energy fluence and for both short and long-term monitoring, we found statistically insignificant differences between the cell populations identified as apoptotic and/or necrotic and the ones identified as necrotic only (Fig. S1†). The latter indicates necrosis as the dominant cell death mechanism.

Previous relevant intracellular delivery studies employed cell incubation with AuNPs and conventional open-space optics to deliver ns laser pulses (λ = 532 nm) to the sample.[33,34] We observed a similar laser fluence processing window compared to these studies. Notably, the optofluidic-based implementation demonstrated here shows that intracellular delivery is feasible without AuNP cell incubation. Considering the low penetration depth (~0.1 to 0.5 mm) of the 532 nm irradiation in tissue,[35] the optofluidic based implementation reported herein can be used to deliver light and intracellular delivery mixtures much deeper (few mm) in soft tissue compared to external irradiation. Given the extensive use of similar probes in optogenetics,[27,36] the developed method could find application in *in vivo* transfection and/or stimulation of neurons.[37,38]

Intracellular delivery in single targeted cells

In the second part of our study, we employed the optofluidic probe to perform intracellular delivery in single targeted cells. We targeted the cells by manually displacing the optofluidic probe and performed irradiation at the optimized laser fluence of 60 mJ cm^{-2}. Groups of individual cells were irradiated with different numbers of pulses.

Fig. 7 shows an indicative single-cell targeting experiment. We targeted 5 groups of 5 cells with 2, 5, 10, 50, and 100 pulses per cell. The dashed circular mark indicates the diameter and positioning of the optofluidic tip during the irradiation step. For a 2-pulse treatment, we observed a decrease in the intracellular delivery efficacy. For treatment with a higher number of pulses, there was no evident effect on the efficacy. We observed 100% targeting specificity when the tip of the optofluidic probe covered only a single cell during the irradiation step. On the other hand, we observed intracellular delivery to neighboring cells when they were partially covered by the tip of the optofluidic probe during the irradiation step (see spots 2, 3, 11, 10, and 16 in Fig. 7).

These results demonstrate the ability to perform single-cell targeted intracellular delivery with a reusable optofluidic probe. Notably, the light and intracellular delivery mixture are being delivered to the sample in a single step. The size of the tip of the optofluidic probe determines the spatial resolution; thus, for future studies dealing with confluent samples, the tip size has to be half the average cell size to ensure efficient single cell targeting.

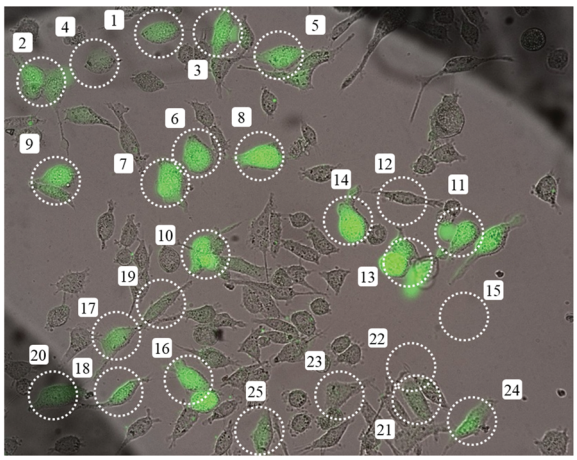

Fig. 7 Targeted intercellular delivery of a green dye in cancer cells using the optofluidic probe and optimized laser fluence (60 mJ cm^{-2}). Groups of cells were treated with different numbers of laser pulses (1–5: 100 pulses; 6–10: 50 pulses; 11–15: 10 pulses; 16–20: 5 pulses; 21–25: 2 pulses). The doted circle indicates the size and position of the tip of the optofluidic probe during irradiation.

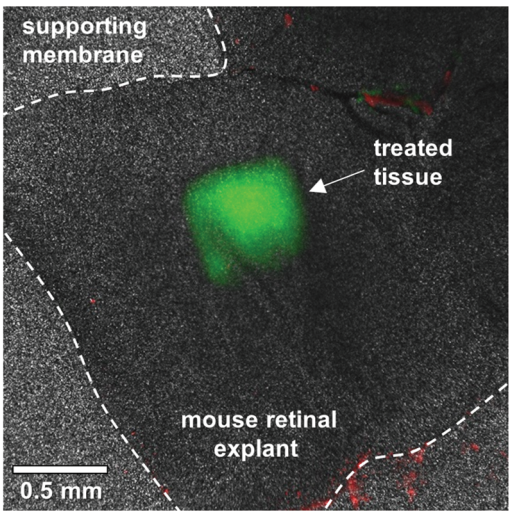

Fig. 8 Intercellular delivery of a green dye within a square region of a mouse retinal explant using the optofluidic probe and optimized laser fluence (60 mJ cm^{-2}). Overlay of fluorescence and transmission images. Representative of 3 experiments.

The Dholakia group has reported intracellular delivery of plasmids using tapered optical fibers coupled to a femtosecond (fs) laser.[39,40] The use of a tapered fiber involves precise adjustment of its focal point on the cell membrane. Compared to this method, the AuNP-assisted approach eliminates the need to tightly focus the exiting beam. Furthermore, it is enabled by ns laser sources which have significantly lower costs and smaller footprints compared to fs laser sources. Ns laser-assisted intracellular delivery has been reported using microcapillaries coated with metallic nanostructures.[41,42] This approach involves contact of the microcapillary with the cell membrane and external illumination of the probe once positioned on the cell membrane. Compared to this method, our approach eliminates the need to use an external beam delivery system and the complexity of bringing the probe in contact with a cell. However, we stress here that a fair comparison on the intracellular delivery efficacy cannot be provided because of the different molecular cargos and cell types used.

Intracellular delivery in mouse retinal explants

The ability to perform targeted delivery of therapeutic compounds within the retinal layers is critical for the development of novel therapies for retinal degeneration diseases.[4] It has been recently shown that laser-irradiated NPs can enable intracellular delivery of siRNA in retinal ganglion cells *in vivo* (rat model).[43] In this context, we consider the back of the eye of small animals as potential field of application for the optofluidic probe. In the third part of our study, we sought to validate this hypothesis *ex vivo*. Prior treatment with the optofluidic probe, we placed the retinal explants into porous membrane cell culture inserts with the ganglion cell side facing up. We incubated 1 h to enhance adhesion and we used the optofluidic probe to treat 0.5 mm × 0.5 mm regions of each explant at optimized laser energy fluence (60 mJ cm^{-2}). We applied similar approaching, injection and irradiation procedures as in the 2D culture experiments. We observed cellular uptake of the green dye within the treated region only (Fig. 8). Importantly, no noticeable cell necrosis was observed within the treated area (Fig. 8).

These results demonstrate that the optofluidic probe enables intracellular delivery of biomolecules in delicate tissue *ex vivo*, such us the mouse retina. Given the eye anatomy and the fact that small animals are commonly used as retinal disease models, the optofluidic probes can be used as an efficient method to deliver intravitreally novel treatments based on photo-activated NPs.

Intracellular delivery mechanism and *in vivo* application implications

The interaction of ns laser pulses with AuNPs can lead to a series of events depending on the incident laser fluence and AuNP size, including AuNP heating, confined cavitation, micro/nano-bubble generation and AuNP disintegration.[13,14] Micro/nano-bubble generation in close proximity to the cell membrane, has been previously reported as the key enabling mechanism for the disruption of the cell membrane in AuNP-assisted intracellular delivery.[15,22,44] We experimentally determined threshold and optimum laser fluence for intracellular delivery to be 30 mJ cm^{-2} and 60 mJ cm^{-2}, respectively. These values lie well above the theoretically-calculated bubble generation thresholds[45] and within the range of the experimentally-reported thresholds[46,47] for a given wavelength, AuNP size and pulse regime. We therefore hypothesize bubble generation and expansion as the main cause of the transient membrane-permeability-enabling intracellular delivery.

Potential *in vivo* applications for a given laser technology requires that the irradiation used is not harmful to animals

and/or humans. The laser fluence range determined in our study for intracellular delivery lies slightly above the maximum permissible exposure for skin (20 mJ cm^{-2}) as reported by the American National Standards Institute (ANSI, Z136 laser safety standards) for the given wavelength and pulse regime. Note that ANSI standards overestimate damage thresholds and laser treatments can exceed these values. For example, laser tattoo removal is being performed at laser fluences 10 to 100-fold higher[48] than those reported here for intracellular delivery. In this context, we anticipate that phototoxicity would not be a limitation for potential *in vivo* intracellular delivery using the optofluidic probe and ns laser pulses.

The axial resolution of the treatment can be estimated as the depth, at which, the beam exiting the optofluidic probe loses 50% of its intensity. For low-absorbing tissue, which represents the farthermost case, the loss is governed by the beam divergence. Given the numerical aperture of the optofluidic probes (NA = 0.23), the axial resolution can be estimated by the following approximate formula $\sim 6 \times D_o$, where D_o is the diameter of the optical core. Thus, tissue or cells placed $<6 \times D_o$ far from the optofluidic probe would receive similar treatment. Small animal *in vivo* implementation can be based on well-established precise injection techniques, such as the use of micromanipulators for subretinal injections[49] and/or the use of stereotaxic systems for brain injections.[50]

Conclusions

We introduced and validated a method to perform intracellular delivery of molecular cargo on live cells by using a reusable, needle-like optofluidic probe capable of penetrating soft tissue. The confined delivery of pulsed laser irradiation and nanomaterials in the vicinity of cells is the key enabling functionality of the probe. Neither precise positioning of the probe on the cell membrane nor cell-nanomaterial incubation is required. Importantly, intracellular delivery was enabled by low energy ns laser pulses, widely available by low cost and small footprint laser sources. Moreover, the method presented here could be potentially implemented with a large variety of optofluidic probes which are currently widespread in the field of optogenetics. It can facilitate *in vivo* treatments in soft tissue of small animals (*e.g.* brain, retina) such us nanomaterial-assisted neuro-stimulation, transfection and tumor elimination.

Conflicts of interest

There are no conflicts to declare.

Acknowledgements

The authors thank Mr C. Boisvert (Polytechnique Montreal) who performed preliminary experiments, Prof. S. Costantino (CR-HMR) for providing access to cell culturing resources, Prof. B. Larrivée (CR-HMR) and Ms N. Popovic (CR-HMR) for providing retinal explants, Prof Y. De Koninck (Université Laval) and Prof. M. Lévesque (Université Laval) for interesting discussions, Dr J. Roy (CR-HMR) for cell culture training and assistance, and Dr M. Sergeev (CR-HMR) for confocal microscopy training and assistance. CB gratefully acknowledges financial support from CR-HMR (start-up funds). CB is the recipient of a salary award from Fonds de la Recherche en Santé du Quebec (FRSQ) (253123 and 265459).

References

1 A. Fu, R. Tang, J. Hardie, M. E. Farkas and V. M. Rotello, *Bioconjugate Chem.*, 2014, **25**, 1602–1608.
2 Y. Zhang, J. J. Røise, K. Lee, J. Li and N. Murthy, *Curr. Opin. Biotechnol.*, 2018, **52**, 25–31.
3 V. P. Torchilin, *Annu. Rev. Biomed. Eng.*, 2006, **8**, 343–375.
4 E. P. Rakoczy, C.-M. Lai, A. L. Magno, M. E. Wikstrom, M. A. French, C. M. Pierce, S. D. Schwartz, M. S. Blumenkranz, T. W. Chalberg, M. A. Degli-Esposti and I. J. Constable, *Lancet*, 2015, **386**, 2395–2403.
5 A. Dinca, W.-M. Chien and M. Chin, *Int. J. Mol. Sci.*, 2016, **17**, 263.
6 R. Waehler, S. J. Russell and D. T. Curiel, *Nat. Rev. Genet.*, 2007, **8**, 573–587.
7 Editorial, *Nature*, 2016, **534**, 590–590.
8 H. Yin, R. L. Kanasty, A. A. Eltoukhy, A. J. Vegas, J. R. Dorkin and D. G. Anderson, *Nat. Rev. Genet.*, 2014, **15**, 541–555.
9 T. G. Iversen, T. Skotland and K. Sandvig, *Nano Today*, 2011, **6**, 176–185.
10 R. Thiruppathi, S. Mishra, M. Ganapathy, P. Padmanabhan and B. Gulyás, *Adv. Sci.*, 2017, **4**, 1600279.
11 M. Riley and W. Vermerris, *Nanomaterials*, 2017, **7**, 94.
12 R. Vankayala and K. C. Hwang, *Adv. Mater.*, 2018, 1706320.
13 E. Boulais, R. Lachaine, A. Hatef and M. Meunier, *J. Photochem. Photobiol., C*, 2013, **17**, 26–49.
14 S. Hashimoto, D. Werner and T. Uwada, *J. Photochem. Photobiol., C*, 2012, **13**, 28–54.
15 R. Lachaine, C. Boutopoulos, P.-Y. Lajoie, É. Boulais and M. Meunier, *Nano Lett.*, 2016, **16**, 3187–3194.
16 C. Boutopoulos, A. Hatef, M. Fortin-Deschênes and M. Meunier, *Nanoscale*, 2015, **7**, 11758–11765.
17 C. Boutopoulos, A. Dagallier, M. Sansone, A.-P. Blanchard-Dionne, É. Lecavalier-Hurtubise, É. Boulais and M. Meunier, *Nanoscale*, 2016, **8**, 17196–17203.
18 C. M. Pitsillides, E. K. Joe, X. Wei, R. R. Anderson and C. P. Lin, *Biophys. J.*, 2003, **84**, 4023–4032.
19 C. Yao, R. Rahmanzadeh, E. Endl, Z. Zhang, J. Gerdes and G. Hüttmann, *J. Biomed. Opt.*, 2005, **10**, 064012.
20 J. Baumgart, L. Humbert, É. Boulais, R. Lachaine, J.-J. Lebrun and M. Meunier, *Biomaterials*, 2012, **33**, 2345–2350.
21 E. Bergeron, C. Boutopoulos, R. Martel, A. Torres, C. Rodriguez, J. Niskanen, J.-J. Lebrun, F. M. Winnik, P. Sapieha and M. Meunier, *Nanoscale*, 2015, **7**, 17836–17847.

22 C. Boutopoulos, E. Bergeron and M. Meunier, *J. Biophotonics*, 2016, **9**, 26–31.
23 M. Schomaker, D. Killian, S. Willenbrock, D. Heinemann, S. Kalies, A. Ngezahayo, I. Nolte, T. Ripken, C. Junghanß, H. Meyer, H. M. Escobar and A. Heisterkamp, *J. Biophotonics*, 2015, **8**, 646–658.
24 D. Heinemann, M. Schomaker, S. Kalies, M. Schieck, R. Carlson, H. Murua Escobar, T. Ripken, H. Meyer and A. Heisterkamp, *PLoS One*, 2013, **8**, e58604.
25 S. Wilhelm, A. J. Tavares, Q. Dai, S. Ohta, J. Audet, H. F. Dvorak and W. C. W. Chan, *Nat. Rev. Mater.*, 2016, **1**, 16014.
26 S. Stolik, J. Delgado, A. Pérez and L. Anasagasti, *J. Photochem. Photobiol., B*, 2000, **57**, 90–93.
27 Y. LeChasseur, S. Dufour, G. Lavertu, C. Bories, M. Deschênes, R. Vallée and Y. De Koninck, *Nat. Methods*, 2011, **8**, 319–325.
28 N. Akla, C. Viallard, N. Popovic, C. Lora Gil, P. Sapieha and B. Larrivée, *Arterioscler., Thromb., Vasc. Biol.*, 2018, **38**, 1821–1836.
29 E. Y. Lukianova-Hleb, A. P. Samaniego, J. Wen, L. S. Metelitsa, C.-C. Chang and D. O. Lapotko, *J. Controlled Release*, 2011, **152**, 286–293.
30 M. Schomaker, D. Heinemann, S. Kalies, S. Willenbrock, S. Wagner, I. Nolte, T. Ripken, H. M. Escobar, H. Meyer and A. Heisterkamp, *J. Nanobiotechnol.*, 2015, **13**, 1–15.
31 T. Mironava, M. Hadjiargyrou, M. Simon, V. Jurukovski and M. H. Rafailovich, *Nanotoxicology*, 2010, **4**, 120–137.
32 A. M. Alkilany and C. J. Murphy, *J. Nanopart. Res.*, 2010, **12**, 2313–2333.
33 B. St-Louis Lalonde, É. Boulais, J.-J. Lebrun and M. Meunier, *Biomed. Opt. Express*, 2013, **4**, 490.
34 C. Yao, X. Qu, Z. Zhang, G. Hüttmann and R. Rahmanzadeh, *J. Biomed. Opt.*, 2009, **14**, 054034.
35 F. H. Mustafa and M. S. Jaafar, *Indian J. Phys.*, 2013, **87**, 203–209.
36 S. Dufour and Y. De Koninck, *Neurophotonics*, 2015, **2**, 031205.
37 J. Yong, K. Needham, W. G. A. Brown, B. A. Nayagam, S. L. McArthur, A. Yu and P. R. Stoddart, *Adv. Healthcare Mater.*, 2014, **3**, 1862–1868.
38 F. Lavoie-Cardinal, C. Salesse, É. Bergeron, M. Meunier and P. De Koninck, *Sci. Rep.*, 2016, **6**, 1–9.
39 X. Tsampoula, K. Taguchi, T. Cizmár, V. Garces-Chavez, N. Ma, S. Mohanty, K. Mohanty, F. Gunn-Moore and K. Dholakia, *Opt. Express*, 2008, **16**, 17007–17013.
40 N. Ma, P. C. Ashok, D. J. Stevenson, F. J. Gunn-Moore and K. Dholakia, *Biomed. Opt. Express*, 2010, **1**, 694–705.
41 T.-H. Wu, T. Teslaa, M. a. Teitell and P.-Y. Chiou, *Opt. Express*, 2010, **18**, 23153–23160.
42 T.-H. Wu, E. Sagullo, D. Case, X. Zheng, Y. Li, J. S. Hong, T. TeSlaa, A. N. Patananan, J. M. McCaffery, K. Niazi, D. Braas, C. M. Koehler, T. G. Graeber, P.-Y. Chiou and M. A. Teitell, *Cell Metab.*, 2016, **23**, 921–929.
43 A. M. Wilson, J. Mazzaferri, É. Bergeron, S. Patskovsky, P. Marcoux-Valiquette, S. Costantino, P. Sapieha and M. Meunier, *Nano Lett.*, 2018, **18**, 6981–6988.
44 L. J. E. Anderson, E. Hansen, E. Y. Lukianova-Hleb, J. H. Hafner and D. O. Lapotko, *J. Controlled Release*, 2010, **144**, 151–158.
45 K. Metwally, S. Mensah and G. Baffou, *J. Phys. Chem. C*, 2015, **119**, 28586–28596.
46 M. Kitz, S. Preisser, A. Wetterwald, M. Jaeger, G. N. Thalmann and M. Frenz, *Biomed. Opt. Express*, 2011, **2**, 291–304.
47 W. C. Vogt, K. A. Wear, J. Pfefer, I. K. Ilev and A. M. Fales, in *Plasmonics in Biology and Medicine XV*, ed. T. Vo-Dinh and J. R. Lakowicz, SPIE, 2018, p. 11.
48 C. Gómez, V. Martin, R. Sastre, Á. Costela and I. García-Moreno, *Arch. Dermatol.*, 2010, **146**, 39–45.
49 P. D. Westenskow, T. Kurihara, S. Bravo, D. Feitelberg, Z. A. Sedillo, E. Aguilar and M. Friedlander, *J. Visualized Exp.*, 2015, e52247.
50 A. Cetin, S. Komai, M. Eliava, P. H. Seeburg and P. Osten, *Nat. Protoc.*, 2007, **1**, 3166.

